

1 **Seasonality of the Mesoscale Inverse Cascade as Inferred from Global**  
2 **Scale-Dependent Eddy Energy Observations**

3 Jacob. M. Steinberg,<sup>a</sup> Sylvia T. Cole,<sup>a</sup> Kyla Drushka,<sup>b</sup> Ryan P. Abernathey<sup>c</sup>

4 <sup>a</sup> *Woods Hole Oceanographic Institution, Woods Hole, Massachusetts, USA*

5 <sup>b</sup> *Applied Physics Laboratory, University of Washington, Seattle, Washington, USA*

6 <sup>c</sup> *Lamont Doherty Earth Observatory of Columbia University, Palisades, New York, USA*

7 *Corresponding author: Jacob Steinberg, jsteinberg@whoi.edu*

8 ABSTRACT: Oceanic mesoscale motions including eddies, meanders, fronts, and filaments com-  
9 prise a dominant fraction of oceanic kinetic energy and contribute to the redistribution of tracers in  
10 the ocean such as heat, salt, and nutrients. This reservoir of mesoscale energy is regulated by the  
11 conversion of potential energy and transfers of kinetic energy across spatial scales. Whether and  
12 under what circumstances mesoscale turbulence precipitates forward or inverse cascades, and the  
13 rates of these cascades, remain difficult to directly observe and quantify despite their impacts on  
14 physical and biological processes. Here we use global observations to investigate the seasonality  
15 of surface kinetic energy and upper ocean potential energy. We apply spatial filters to along-track  
16 satellite measurements of sea surface height to diagnose surface eddy kinetic energy across 60-300  
17 km scales. A geographic and scale dependent seasonal cycle appears throughout much of the  
18 mid-latitudes, with eddy kinetic energy at scales less than 60 km peaking 1-4 months before that at  
19 60-300 km scales. Spatial patterns in this lag align with geographic regions where the conversion  
20 of potential to kinetic energy are seasonally varying. In mid-latitudes, the conversion rate peaks  
21 0-2 months prior to kinetic energy at scales less than 60 km. The consistent geographic patterns  
22 between the seasonality of potential energy conversion and kinetic energy across spatial scale  
23 provide observational evidence for the inverse cascade, and demonstrate that some component of  
24 it is seasonally modulated. Implications for mesoscale parameterizations and numerical modeling  
25 are discussed.

26 This study investigates the seasonality of upper ocean potential and kinetic energy in the context  
27 of an inverse cascade, consisting of energy transfers to and through the mesoscale. Observations  
28 show a scale-dependent cycle in kinetic energy that coincides with temporal variability in mixed  
29 layer potential energy and progresses seasonally from smaller to larger scales. This pattern appears  
30 dominant over large regions of the ocean. Results are relevant to ocean and climate models, where  
31 a large fraction of ocean energy is often parameterized. A customizable code repository and  
32 dataset are provided to enable comparisons of model-based resolved and unresolved kinetic energy  
33 to observational equivalents. Implications result for a range of processes including mixed layer  
34 stratification and vertical structure of ocean currents.

## 35 1. Introduction

36 Mesoscale turbulence represents a dominant fraction of ocean kinetic energy (KE) and consists  
37 of flows that evolve on  $O[10 - 300]$  km spatial scales and week to month time scales (Ferrari  
38 and Wunsch 2009). Motions outside of these spatio-temporal bounds can act as sources or  
39 sinks of this mesoscale energy. For instance, instabilities of western boundary currents can  
40 generate smaller-scale fluctuations like Gulf Stream rings; mesoscale eddies can break apart into  
41 smaller filaments with shorter space and time scales; an inverse cascade can import energy from  
42 submesoscales ( $O[1 - 10]$  km); and mesoscale motions can merge with mean flows. Efforts to  
43 model the ocean and climate system crucially depend on energy transfers within and through the  
44 mesoscale range, with such motions either parameterized or only partially resolved in numerical  
45 models. The inverse cascade at mesoscales is one component of a two-part energy cycle: first,  
46 available potential energy (PE) is converted to kinetic energy at instability scales, and second,  
47 kinetic energy at small scales is transferred to kinetic energy at larger scales. This idealized  
48 description of an inverse cascade, however, assumes the flow to be balanced, with competing  
49 dynamics playing a minimal role. In reality only some fraction of small scale KE moves to larger  
50 scales. The inverse cascade of KE from submesoscales to mesoscales to larger scales is predicted  
51 and required by quasi-two-dimensional geostrophic turbulence theory and assumes a steady-state  
52 balance between production and dissipation (Kraichnan 1967; Charney 1971; McWilliams 1989).  
53 It occurs in the ocean alongside forcings that act across a range of scales and unbalanced motions  
54 that can simultaneously precipitate a forward cascade towards dissipation (Roullet et al. 2012). A

55 main source of KE at submeso- and mesoscales is available potential energy stored in the upper  
56 ocean. This potential energy reservoir, larger in winter due to deepened mixed layers and stronger  
57 horizontal density gradients, is a source of kinetic energy converted via baroclinic instability at  
58 scales near to or smaller than the first baroclinic deformation radius (Smith and Vallis 2001; Mensa  
59 et al. 2013; Sasaki et al. 2014; Callies et al. 2015, 2016; Dong et al. 2020a). Along with horizontal  
60 density gradients and mixed layer depths, the conversion of potential to kinetic energy varies  
61 seasonally, with mixed layer eddies generated via frontal adjustment contributing to springtime  
62 vertical restratification (Johnson et al. 2016). Modeling studies have shown this frontal adjustment  
63 mechanism for generating eddies at submesoscales to act as a key source of mesoscale energy  
64 evolving on both seasonal and longer time scales (e.g., Fox-Kemper et al. 2008).

65 While the inverse cascade across mesoscales itself has been infrequently observed, its result  
66 has been inferred from observations revealing eddy energy-containing scales to be larger than  
67 predicted instability scales (Chelton et al. 2007). The inverse cascade is further complicated in  
68 a three-dimensional ocean with variable vertical stratification, but modeling studies have shown  
69 that an inverse cascade does occur in both barotropic and baroclinic modes and across a range of  
70 wavenumbers between instability scales and the Rhines' scale (Scott and Arbic 2007; Serazin et al.  
71 2018). Direct observations of these kinetic energy fluxes, however, are limited to either select  
72 locations or across spatial scales greater than  $\sim 150$  km (Scott and Wang 2005; Callies and Ferrari  
73 2013).

74 Space-borne observations of sea surface height (SSH) provide a means of quantifying ocean KE  
75 and eddy kinetic energy (EKE) globally. These measurements have long been used to characterize  
76 ocean energetics (Stammer and Dieterich 1999; Scott and Wang 2005; Chelton et al. 2007, 2011;  
77 Xu and Fu 2012; Arbic et al. 2013; Rocha et al. 2016), develop eddy censuses (Chelton et al. 2011),  
78 and determine the spectral flux of KE across mesoscales (Scott and Wang 2005; Arbic et al. 2014).  
79 Analyses often partition ocean KE into time-mean and varying components and/or use gridded  
80 altimetry products that reduce horizontal resolution to  $\sim 150$  km due to smoothing associated with  
81 interpolation (Taburet et al. 2020). Individual satellite altimeters offer higher spatial resolution, but  
82 are still limited by along-track altimeter resolution relative to a latitudinally-dependent eddy length  
83 scale, instrument noise, track repeat time, and spatial gaps between adjacent tracks. Despite these  
84 limitations, recent along-track analysis by Chen and Qiu (2021) show their utility by quantifying



85 the fraction of SSH variability at scales unresolved by gridded products, using spectral methods to  
86 partition variance, and finding seasonality in this signal.

87 Here, a framework is constructed to capitalize on the availability of high resolution along-track  
88 measurements and to apply a scale-aware spatial filtering method. We determine the partitioning of  
89 energy across 60-300 km horizontal scales and seasons globally. The methods developed and used  
90 in this analysis uniquely permit KE to be partitioned across mesoscales without needing to choose  
91 interpolation parameters, such as spatial and temporal decorrelation scales, and windowing or  
92 tapering scales required in spectral analysis. These methods complement and extend those of Chen  
93 and Qiu (2021) by considering EKE, employing different methods of spatial filtering, interpreting  
94 results alongside observations of upper ocean potential energy, and reconciling seasonal patterns  
95 with mesoscale turbulence theory. Results reveal regions in the ocean where an imprint of the  
96 inverse cascade is apparent, specifically where a seasonal imbalance in the PE to EKE conversion  
97 rate appears linked to a scale-dependent seasonal cycle in mesoscale KE. This increased level  
98 of spatio-temporal detail regarding the partitioning of KE within the ocean is a crucial part of  
99 understanding ocean dynamics and whether numerical models, from regional simulations to global  
100 climate models, correctly represent oceanic processes.

## 101 2. Data

102 As provided by the Copernicus European Earth Observation program [<https://marine.copernicus.eu>], SSH measurements from three altimeter missions are considered, including  
103 a twenty-year multi-satellite-derived mean sea surface (MSS) estimate. These data are accessed  
104 via Pangeo, a cloud-based platform with ready-to-analyze large datasets, such that analysis tools  
105 developed here can be used by the community without individually downloading and processing  
106 locally. Here we primarily consider measurements from the Jason-2 mission (j2), with minor  
107 comparisons to SARAL-AltiKa (al) and Sentinel-3A (s3a). In all cases, we use a pre-processed  
108 low-pass filtered variable, 'sla\_filtered', which minimizes instrument error (average SSH error of  
109 j2=1.1, al=0.8, s3a=0.9 cm rms) and has an approximate horizontal resolution of 50, 40, and 40 km  
110 for the three satellites, respectively (Taburet et al. 2020; Dufau et al. 2016). Jason-2 measurements  
111 represent the longest available measurement time series of  $\sim 8$  years (2008-2015). SARAL-AltiKa  
112 and Sentinel-3A altimeters are both more accurate, with lower rms instrument noise, but occupy  
113

orbital tracks less frequently. For additional differences among altimeters, including seasonality in instrument error, see Dufau et al. (2016). Authors specifically highlight altimeter limitations in the Southern Ocean, a region included in this analysis, and confirm resolution capabilities down to  $O[50\text{km}]$ . While differences in altimeter instrument accuracy and mission duration motivate separate analysis for each satellite, statistical properties and spatial patterns of eddy variability are comparable.

Two products derived from Argo float observations are used to estimate the conversion rate of potential to kinetic energy. The first is a database of monthly temperature and salinity profiles on a  $1^\circ \times 1^\circ$  grid, created using Argo float profiles collected between 2007 and present (Roemmich and Gilson 2009). The second provides mean monthly mixed layer depth and densities (Holte et al. 2017), and is used to vertically partition density profiles from Roemmich and Gilson (2009). These data products represent the climatological state of mesoscale and larger ocean properties.

### 3. Analysis Framework

#### *a. Scale-Aware Eddy Kinetic Energy*

The following analysis does not attempt to resolve individual eddy features, but rather geographic and seasonal patterns in velocity variance and eddy kinetic energy. Briefly, we construct a general spatial filtering framework designed to filter any variable along a single spatial dimension. This framework is then applied to cross-track estimates of geostrophic velocity calculated from along-track gradients of absolute dynamic topography (ADT). We then partition observed variance into mean and eddy kinetic energy components. While SSH variance can be estimated at a relatively finer horizontal resolution without having to calculate a gradient (and is also useful for model validation purposes), we focus here on eddy energetics.

#### 1) GEOSTROPHIC VELOCITY

The along-track SSH measurements used here are all available with 7 km spacing. Data are first linearly interpolated to 20 km spacing and across intermittent data gap segments of less than 50 km. The choice of 20 km spacing improves the implementation of the spatial filter introduced below. ADT,  $\eta(x, t)$ , represents the dynamical component of the satellite measurement and is defined everywhere as

$$\eta(x, t) = SSH - MSS + MDT = SSH - MSS + (MSS - Geoid) = SSH - Geoid \quad (1)$$

where, for each unique track,  $x$  is along-track distance in meters,  $t$  time, MSS the temporal mean sea surface height, and mean dynamic topography MDT is the temporal mean of SSH above the geoid (Pujol and Mertz 2020). The geoid is the baseline surface height of the ocean under the influence of gravity and rotation alone and is included in the MDT estimate. Cross-track geostrophic velocity  $u$  is then estimated as

$$u(x, t) = \frac{g}{f} \frac{\partial \eta}{\partial x} \quad (2)$$

where  $g = 9.81 \text{ m/s}^2$  and  $f$  is the local Coriolis frequency. A negative sign is omitted as we consider only the magnitude of cross-track velocity and its spatial and temporal variability. The along-track gradient of ADT is estimated using a 3-point center difference gradient stencil (Arbic et al. 2012).

Cross-track velocities are calculated for each cycle of each track (Fig. 1a,b) of the desired altimeter. The assumption that these estimates equally represent zonal and meridional components of an isotropic field is justified based on consistency among three altimeters having different orbital track geometries. Comparisons between these estimates and gridded velocities produced by AVISO (not shown) reveal significant differences, largely due to the increased horizontal resolution at which KE can be estimated using along-track measurements.

## 2) MEAN AND EDDY KINETIC ENERGY

We use spatial filtering to decompose geostrophic velocity into contributions from eddying motions at specific spatial scales. Specifically, for a spatial filter of length  $l$  denoted by  $\langle \rangle_l$ , the eddy kinetic energy at scales smaller than the filter scale (EKE) and mean kinetic energy at scales larger than the filter scale (MKE) are:

$$EKE_l = \tau(u, u)_l = \langle u^2 \rangle_l - \langle u \rangle_l^2 \quad (3)$$

$$MKE_l = \langle u \rangle_l^2, \quad (4)$$

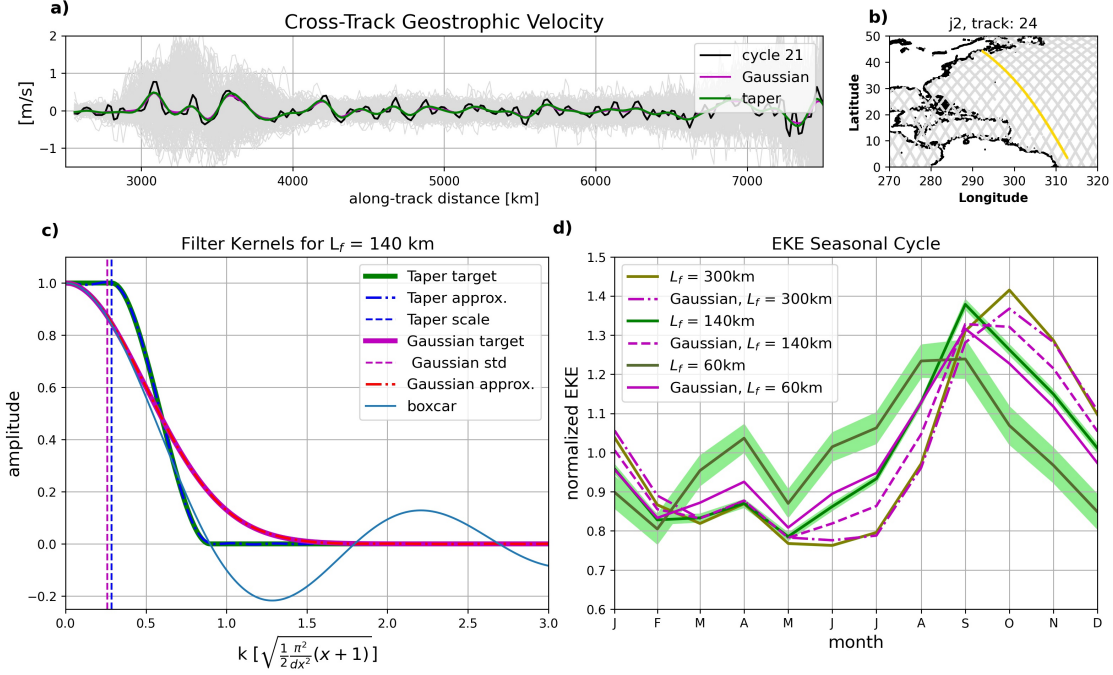


FIG. 1. a) Cross-track geostrophic velocities (grey) as a function of along-track distance along the Jason-2 altimeter track 24 from 2008-2015 (258 cycles). Track 24 and cycle 21 (black) is selected as an example and filtered using the Gaussian (purple) and taper (green) filters to 140 km. b) Path over ground of Jason-2 tracks with track 24 in yellow. Along-track distance increases north to south. c) Fourier transform of boxcar (blue), target and approximate Gaussian (purple), and target and approximate taper (green) filter kernels for a 140 km filter. Horizontal axis is the normalized horizontal wavenumber with  $dx$  and  $x$  the grid spacing and grid indices. Vertical lines identify the normalized filter scale. d) Seasonal cycle in EKE at  $[92^\circ\text{E}, 19^\circ\text{S}]$  for three filter scales (60, 140, 300 km) and two filter types: taper (green) and Gaussian (purple). EKE at each scale is normalized by its annual mean. The shaded regions are the standard deviation of 250 Monte Carlo simulations showing the effect of random instrument error added to absolute dynamic topography measurements.

where small-scale variance  $\tau$  is defined as  $\tau(u, u)_l = \langle u^2 \rangle_l - \langle u \rangle_l^2$  following Germano (1992), Aluie et al. (2018), and Sadek and Aluie (2018). Note that these estimates exclude an along-track velocity component and that a factor of  $\frac{1}{2}$  is implicit in estimates of KE. This follows from the assumption that the geometries of altimeter orbital tracks result in adequate sampling of both zonal and meridional components of the surface velocity field, and that they are isotropic. This framework prevents the need to define an anomaly quantity (i.e.,  $u' = u - \langle u \rangle$ ) and the need to

177 address the magnitude of cross terms (i.e.,  $\langle u \rangle u'$ ) following substitution into momentum equations.  
 178 The partitioning of variance into large- and small-scale bins is then framed about the filter scale  
 179  $l$ . In practical terms, this filtering framework prescribes set scales across which variance can be  
 180 partitioned, analogous to resolvable and sub-grid variance in an ocean model.

181 The energy or variance of a field can also be decomposed into  $N$  distinct bands. Let  $\gamma_n$  be the  
 182 operator that isolates a band. For a single filter, MKE and EKE are given by:

$$MKE = \sum_{n=1}^j \gamma_n(u^2) = \langle u \rangle_{\ell_j}^2 \quad (5)$$

$$EKE = \sum_{n=j+1}^N \gamma_n(u^2) = \langle u^2 \rangle - \langle u \rangle_{\ell_j}^2 = \tau(u, u) \quad (6)$$

183 where the angle brackets represent the convolution with a filter of length scale  $\ell_1$ . This acts as a  
 184 low-pass filter, passing variance at scales larger than  $\ell_1$ . For two filter scales, energy within a band  
 185 bounded by scales  $\ell_1$  and  $\ell_2$  (i.e., a band pass filter) is

$$\gamma_2(u^2) = \langle u \rangle_{\ell_2}^2 - \langle u \rangle_{\ell_1}^2. \quad (7)$$

186 For  $N$  bands, we want this to satisfy the integral constraint that

$$\int u^2 dx = \sum_{n=1}^N \int \gamma_n(u^2) dx. \quad (8)$$

187 The largest-scale energy is defined as

$$\gamma_1(u^2) = \langle u \rangle_{\ell_1}^2. \quad (9)$$

188 This continues until the highest bands (smallest filter scales):

$$\gamma_{N-1}(u^2) = \langle u \rangle_{\ell_{N-1}}^2 - \langle u \rangle_{\ell_{N-2}}^2 \quad (10)$$

$$\gamma_N(u^2) = u^2 - \langle u \rangle_{\ell_{N-1}}^2 \quad (11)$$

189 where the last band,  $\gamma_N(u^2)$ , is the high-pass filtered energy. For this decomposition, it is straight-  
 190 forward to show that

$$\sum_{n=1}^N \gamma_n(u^2) = u^2. \quad (12)$$

191 This decomposition of velocity variance into  $N$  distinct bands reveals the partitioning of kinetic  
 192 energy across scales and serves as a discrete analogue to the wavenumber spectra (Sadek and Aluie  
 193 2018).

### 194 3) IMPLEMENTATION

195 Following methods employed by Grooms et al. (2021), a spatial filter is applied to velocity from  
 196 each cycle of each altimeter track as a convolution of a desired filter kernel with  $u$  as

$$\langle u(x, t) \rangle_l = G_l * u(x, t), \quad (13)$$

197 where  $G_l$  represents a general filter kernel of width  $l$  with  $n$  number of measurements that span the  
 198 distance  $l$ . For  $l = 5$  and along-track velocity interpolated to a 20 km grid, the filter would have  
 199 zero variance at scales less than 100 km. Three filter kernels are considered: boxcar, Gaussian,  
 200 and taper, each defined to have comparable length scales for a single input  $l$  (Fig. 1). The boxcar  
 201 filter kernel most simply applies this filtering framework and has a uniform set of weights of width

$$L_f = n\Delta_x \quad (14)$$

202 where  $L_f$  is the filter width more generally defined above as  $l$ ,  $\Delta_x$  is the grid step, and filter weights  
 203 are  $1/n$ . A Gaussian kernel of the same characteristic scale takes the form

$$G_{L_f}(x) = e^{-6|x/L_f|^2}. \quad (15)$$

204 This expression was selected by considering the Fourier transform of both the boxcar and Gaussian  
 205 filters and identifying first zero crossings. Equivalently, the taper filter is designed to eliminate  
 206 contributions from wavenumbers  $k$  greater than  $2\pi/L_f$ . These diffusion-based Gaussian and taper  
 207 filters employ Laplacian and biharmonic operators to iteratively approximate a target step-like filter

constructed in Fourier space using Chebyshev polynomials (Fig. 1). Stability of this smoothing technique is ensured for filtering scales generally less than 50 times larger than the grid scale and is here no larger than 15 (Grooms et al. 2021).

To make this filtering framework both dynamically relevant and useful in an observational-model comparison, the filter scale  $l$  can be defined in one of three ways: a fixed length scale (e.g., 100 km), a scale tied to a model grid scale (e.g.,  $1^\circ$ ), or a scale tied to a varying dynamical scale (e.g., the first deformation radius  $L_{d1}$ ). The majority of this analysis uses a fixed filter scale and the taper kernel. A fixed length scale is most appropriate for deriving physical meaning from the decomposition of EKE into contributions across scales. After estimating total resolvable KE and filtering all cross-track velocity estimates using the taper filter and a fixed length scale, global maps of KE, MKE, and EKE are constructed by bin-averaging along-track fields within  $4^\circ \times 4^\circ$  bins on a  $1^\circ$  longitude-latitude grid (Fig. 2).

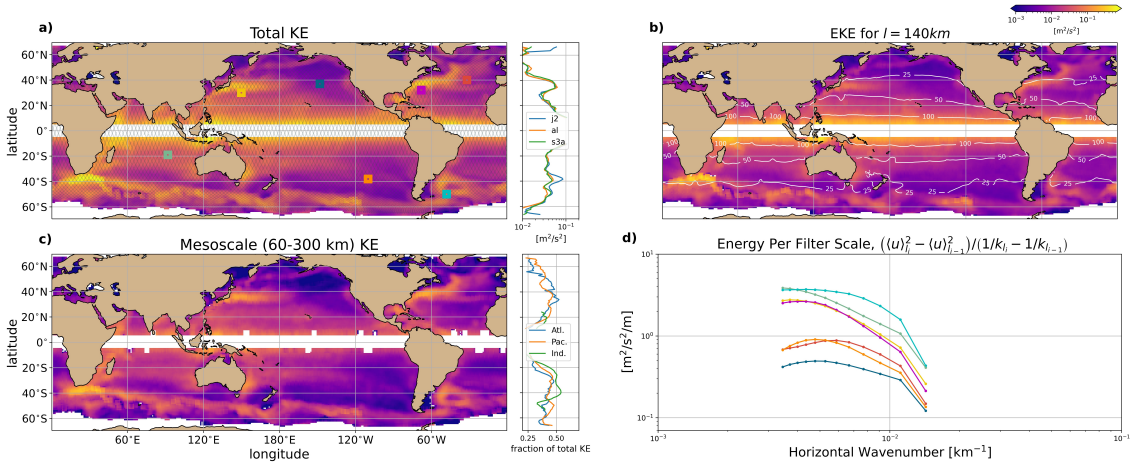


FIG. 2. Gridded maps of a) mean total kinetic energy from Jason-2 (2009-2016) cross-track geostrophic velocity estimates, b) Mean eddy kinetic energy at scales less than 140 km with the first baroclinic deformation radius contoured in white, and c) Mean kinetic energy within the 60-300 km band (Eq. 3). Colored boxes identify seven select locations individually considered. In (a), zonal mean total kinetic energy for Jason-2 (blue), SARAL-Altika (orange), and Sentinel-3a (green) altimeters is also shown. In (c), the zonal average of KE within the 60-300 km band for the Atlantic (blue), Indian (green), and Pacific (orange) basins is shown as a fraction of mean total KE. d) Kinetic energy within the 60 - 300 km band at the seven locations identified in (a). Estimates are normalized by band width.

#### 4) ERROR PROPAGATION

While a filter kernel can be selected to minimize spectral leakage, time-varying instrument error reduces confidence in a seasonal analysis. In order to approximate the effect of this temporal variability and gain confidence in these results, normally distributed random errors in ADT were added to each cycle of all tracks falling within a  $10^\circ \times 10^\circ$  box (Fig. 2a: green site indicates box center location). For each cycle of each track, 250 Monte-Carlo simulations were run, adding random error with a standard deviation equal to the maximum seasonal change in SSH error (Dufau et al. 2016). Cross-track geostrophic velocities were then estimated, filtering applied, and EKE estimated at three scales. The standard deviation of these 250 runs (shaded green regions in Figure 1d) reveals added uncertainty in the observed EKE estimate and its scale-dependent seasonal cycle. The signal that we subsequently diagnose, a temporal lag in peak EKE at different scales, is further detailed in the upcoming sections, but remains significant with confidence bounds of approximately  $\pm 1$  month. The effect of this seasonal instrument noise decreases many-fold with increasing filter scale. Monte-Carlo error analyses carried out at two additional sites in the North Pacific (not shown) exhibit similar standard deviations across 250 runs and suggest these error estimates are representative despite expected spatial variability in instrument errors.

##### *b. Available Potential Energy and Conversion to Kinetic Energy*

We estimate the mean conversion rate of PE to EKE,  $\overline{w'b'}$ , using an often employed parameterization since it is not possible to directly estimate it from observations. The parameterization of Fox-Kemper et al. (2008) and Fox-Kemper et al. (2011) diagnoses a PE to EKE conversion rate as:

$$\overline{w'b'} = \frac{\Delta s}{L_f} \frac{H^2}{|f|} \left( \left( \frac{\partial b}{\partial x} \right)^2 + \left( \frac{\partial b}{\partial y} \right)^2 \right), \quad (16)$$

where  $H$  is the mixed layer depth,  $f$  is again the local Coriolis parameter, and buoyancy  $b = -g(\rho - \rho_0)/\rho_0$ . The first term in this equation,  $\frac{\Delta s}{L_f}$  is a scaling factor recommended by Fox-Kemper et al. (2011) to account for the sensitivity of this estimate to the distance ( $\Delta s$ ) over which horizontal buoyancy gradients are estimated relative to the horizontal scale of mixed layer instability ( $L_f = NH/|f| \approx |\nabla_h b|H/f^2$ ). These choices are intended to produce an estimate representative of mesoscale fronts that drive mixed layer instabilities (Johnson et al. 2016; Uchida et al. 2017).



Johnson et al. (2016) characterize these large-scale gradients as comprised of smaller-scale and sharper-gradient fronts susceptible to baroclinic instability, while Uchida et al. (2017) use a high-resolution model to show that conversion estimates calculated from time-dependent mesoscale gradients are representative of direct flux estimates. Overall, this parameterization reveals when and where available potential energy stored in mixed layer fronts is converted to EKE via mixed layer baroclinic instability.

We use Argo-derived upper ocean density climatologies to estimate the horizontal buoyancy gradients and mixed layer depths needed for Equation 16. Horizontal buoyancy gradients are estimated at 19 m depth and across 2 degree distances. In Equation 16,  $\Delta s$  varies latitudinally as the distance, in meters, of 2 degrees of longitude, and the length scale of instability  $L_f$  has typical values of a few hundred meters to a few kilometers. Two locations, one in the western North Atlantic and one in the western South Atlantic, highlight the distinct seasonal cycles of mixed layer depth, horizontal buoyancy gradients, and PE to EKE conversion (Fig. 3). In particular they show the differing contributions to this conversion estimate of horizontal buoyancy gradient changes and mixed layer depth changes. These sites were selected to highlight differences in upper ocean seasonality. While mixed layer depths at the South Atlantic site change seasonally by almost 200 m, horizontal buoyancy gradients are weaker such that the conversion rate has a similar peak amplitude to the site in the North Atlantic, where mixed layer depth changes are smaller and horizontal buoyancy gradients stronger. In both cases, the seasonal change in conversion rate is comparable to or larger than the annual mean conversion rate.

## 4. Results

### *a. Mesoscale Eddy Kinetic Energy Across Seasons and Scales*

By filtering geostrophic velocities using the taper filter, we estimate mean kinetic energy (MKE) and EKE across different horizontal scales and seasons. We calculate MKE (Eq. 4) and EKE (Eq. 3) at length scales  $l = 60\text{-}300$  km in 20 km intervals and first generate global maps of KE (Fig. 2a), MKE, and EKE (shown for  $l = 140$  km in Figure 2b). KE within the 60-300 km band is estimated by summing across wavenumbers spanning our chosen filtering band (Fig. 2c,d).

Several aspects of kinetic energy are geographically variable (e.g., Figure 2). Consistent with prior studies, total KE in the Antarctic Circumpolar Current and western boundary current regions

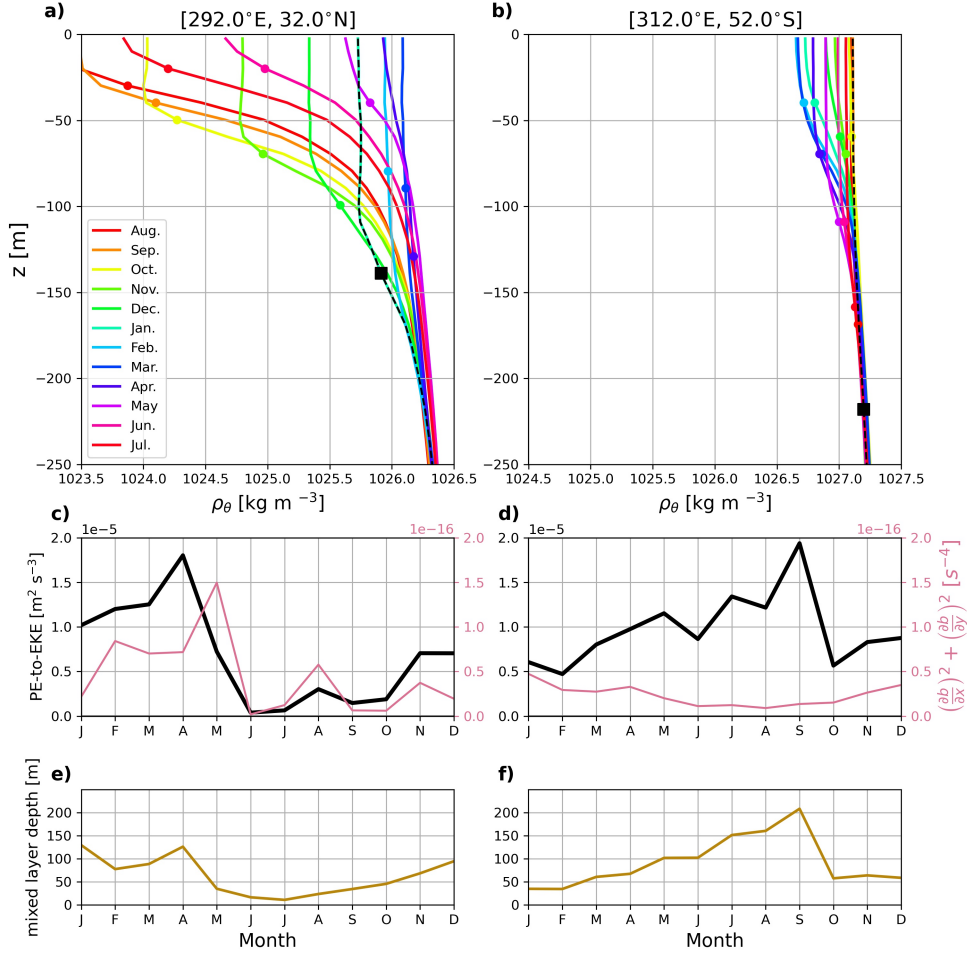


FIG. 3. a-b) Upper ocean density profiles for each month in a) the western north Atlantic Ocean [292°E, 32°N], and b) the southwestern Atlantic Ocean [312°E, 52°S] from Argo float observations (Roemmich and Gilson, 2009). Colored circles identify mixed layer depth for each month with the black square denoting the deepest mixed layer depth. The black dashed line is the corresponding density profile. c-d) Seasonal cycle of the PE to EKE conversion rate (black; Eq. 16) and sum of squared horizontal buoyancy gradients (pink) at c) [292°E, 32°N] and d) [312°E, 52°S]. e-f) Seasonal cycle of mixed layer depth at e) [292°E, 32°N] and f) [312°E, 52°S].

is over an order of magnitude more energetic than in eastern ocean basins. MKE, or the energy at and above a certain filter scale, generally decreases with increasing filter length scale, but the

291 rate of this decrease, akin to a spectral slope, also varies with location (Fig. 2d). Within the  
292 60-300 km range, here defined as the mesoscale band, slopes are steeper where eddy energy is  
293 high. In other words, the partitioning of energy across scales varies geographically. The result  
294 is a varying fraction of KE contained within the mesoscale band, with values approaching 50%  
295 of total resolvable KE in western boundary current regions (Fig. 2c). The fraction of energy  
296 contained in this mesoscale band decreases near the equator and at latitudes greater than  $\sim 45^\circ$ ,  
297 where deformation radii fall outside the upper (equator) and lower (high-latitude) limits of our  
298 60-300 km band.

299 Seasonal variability is first considered by estimating the fraction of KE within two wavelength  
300 bands (60-140 km and 140-300 km) in late Northern Hemisphere winter (Feb. - Apr.) and summer  
301 (Jul. - Sept.) months (Fig. 4a,b,d,e). These months were selected to align with months of  
302 maximal and minimal KE at scales less than 140 km. In the Northern Hemisphere, the fraction of  
303 energy at 60-140 km scales is elevated outside of western boundary current regions, and is overall  
304 larger in wintertime (Fig. 4c). At 140-300 km scales, western boundary current regions have a  
305 larger fraction of energy at these scales during summertime (Jul-Sept in the Northern Hemisphere,  
306 Feb-April in the Southern Hemisphere; Fig. 4d,e). From this basic partitioning, it is clear that  
307 the seasonality of ocean kinetic energy is scale dependent (i.e., it differs at large and small spatial  
308 scales).

311 The largest winter-to-summer differences of approximately 25% variation occur in the 60-140  
312 km band, equatorward of western boundary currents (Fig. 4c). The finding that energy at 60-140  
313 km scales peaks in late winter is consistent with the theory that submesoscale EKE can act as a  
314 time-dependent source of mesoscale EKE that reaches the mesoscale via the inverse cascade (Qiu  
315 et al. 2014; Callies et al. 2015; Uchida et al. 2017; Dong et al. 2020b). At 140-300 km scales,  
316 differences between winter (FMA) and summertime (JAS) KE are smaller in magnitude (Fig. 4f),  
317 as the months of maximal and minimal KE at these scales often occur in other months such that these  
318 winter and summer time periods do not represent the full seasonal change. The Agulhas Current  
319 region is an exception, with significantly elevated KE in Southern Hemisphere winter, consistent  
320 with prior studies (Matano et al. 1998). Overall, this observed seasonality compares favorably to  
321 previous observational studies, which have been limited to analysis of a single mesoscale range  
322 typically larger than 150 km (e.g., Scharffenberg and Stammer (2010)).

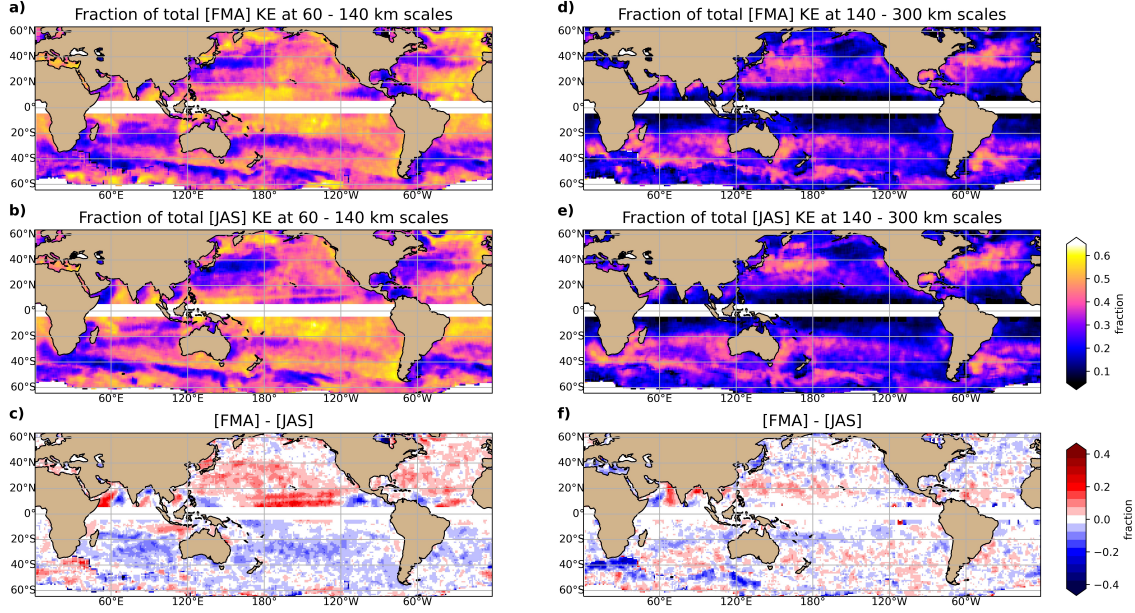


FIG. 4. Fraction of a) FMA and b) JAS total kinetic energy in the 60-140 km band. c) FMA fraction minus JAS fraction. d-f) as in a-c but for 140-300 km scales.

A mean seasonal cycle for each filter scale is constructed by partitioning filtered velocities from all altimeter tracks into monthly bins before averaging into latitude-longitude bins. Seven locations spanning all ocean basins are selected to highlight the mean seasonal cycle for three filter scales (60, 140, 300 km; Fig. 5). At a subset of these example locations (Fig. 5e,g,h), a progression in the month of maximum EKE is identified, with the peak occurring first at small (60 km), then medium (140 km), and finally large (300 km) scales. This progression reveals a scale-dependent shift in the seasonal cycle of EKE, with the difference in peak EKE month identified as a temporal lag. Among the selected sites, not all exhibit this sequence of events (Fig. 5c,d,f,i). At these locations, a seasonal cycle is often observed but is similar at all spatial scales (peak EKE occurs in the same month). These examples show that the amount of total KE does not determine whether or not a region exhibits a scale-dependent shift in the seasonal cycle of EKE.

To investigate global patterns, we consider the peak month of  $EKE_{\leq 60km}$  (Fig. 6b),  $EKE_{60-300km}$  (Fig. 6c), and PE to EKE conversion rate (Fig. 6a). At many locations, a seasonal progression from  $EKE_{\leq 60km}$  to  $EKE_{60-300km}$  is apparent (Fig. 6b,c), even in regions with relatively little total KE (Fig. 2a). At scales less than 60 km, peak EKE occurs in wintertime months. At 60-300 km

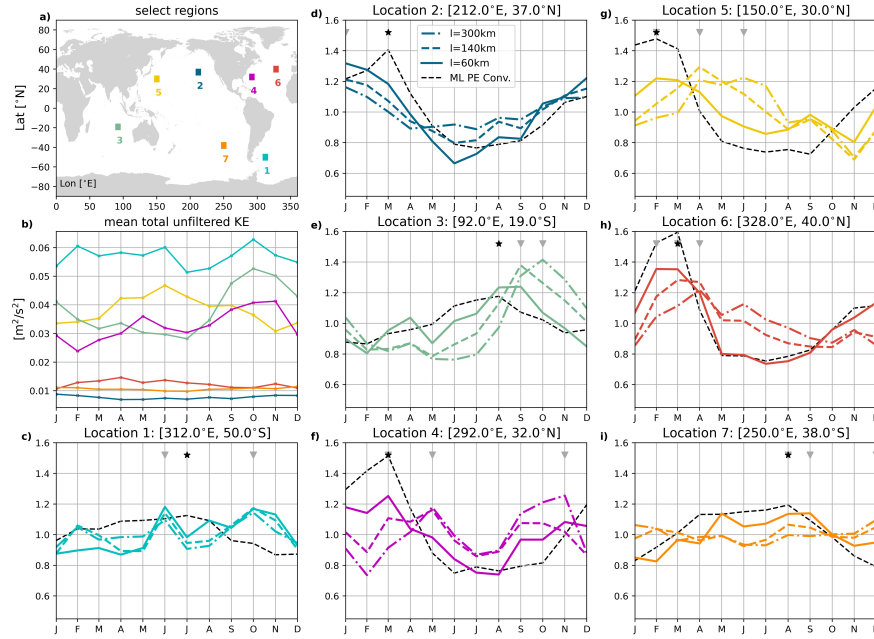


FIG. 5. Mean seasonal cycle as a function of scale at seven select locations (same locations as in Fig. 2). a) Map of locations. b) Mean seasonal cycle of total kinetic energy at each location. c-i) Mean seasonal cycle of eddy kinetic energy normalized by its annually averaged value for 300 (dash-dot), 140 (dash), and 60 (solid) km filter scales. Black line (dashed) is the normalized PE to EKE conversion rate. Symbols identify the month of peak conversion (star) and peak EKE<sub>60km</sub>, EKE<sub>140km</sub>, and EKE<sub>300km</sub> (downward triangles).

scales, spatial variability in the month of maximal EKE is more pronounced, with western boundary current regions peaking several months later than neighboring gyre regions. The difference in the month of maximal EKE<sub>≤60km</sub> and maximal EKE<sub>60–300km</sub> (Fig. 6e) reveals large-scale geographic patterns in a scale-dependent seasonal cycle of EKE. Throughout much of the mid-latitudes,  $\sim 20^\circ$  -  $40^\circ$ , as well as in the sub-polar North Atlantic, this lag is positive and between 1 and 4 months (Fig. 6e, orange regions). Lags are only shown where the amplitude of the seasonal cycle exceeds 25% of its annual mean value, a criteria satisfied at  $\sim 95$  percent of locations. Lags appear greatest in the eddy recirculation region of the subtropical gyres, compared to the eastern North Pacific or South Atlantic where lags approach zero or do not have a definitive sign. Regions with lags outside

of the 1 to 4 month range are found closer to the equator, in the North Pacific north of  $40^{\circ}\text{N}$ , and south of  $45^{\circ}\text{S}$  where deformation radii are outside the 60-300 km scale range considered here.

In summary, large regions of the global ocean, with both high and low levels of mesoscale KE, appear to experience a seasonal cascade of energy from the smallest scale resolvable by the altimeter to  $\sim 300$  km scales. Here, the observed difference in seasonal cycles between  $\text{EKE}_{60-300\text{km}}$  and  $\text{EKE}_{\leq 60\text{km}}$  (Fig. 6) reveals a temporal lag consistent with predictions as to the inverse cascade and prior modeling results (Qiu et al. 2014; Dong et al. 2020b).

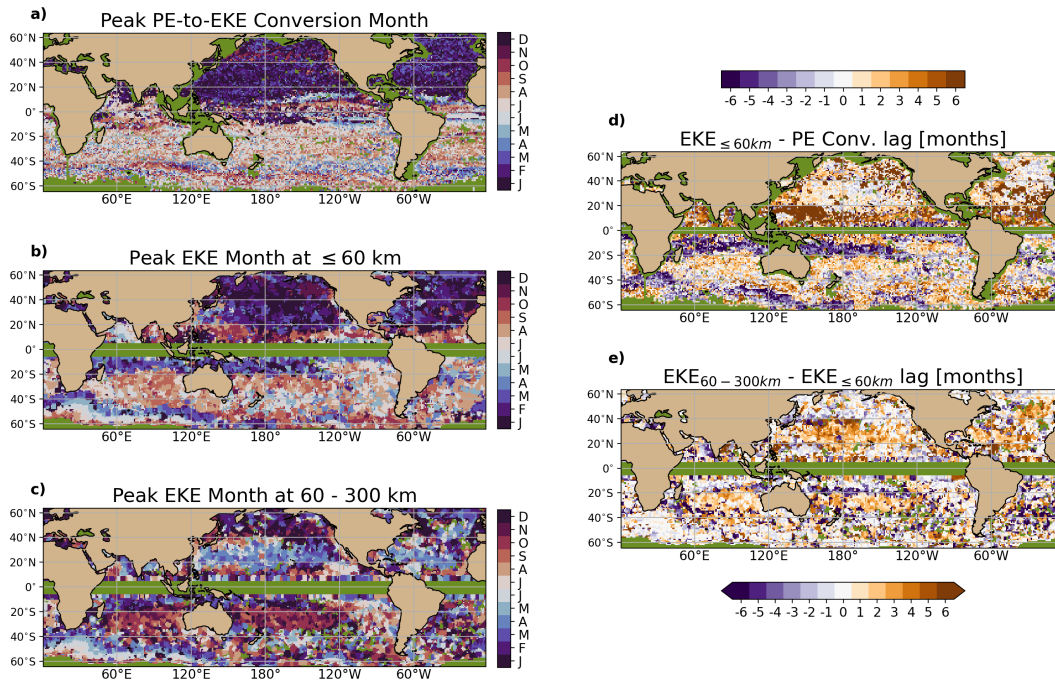


FIG. 6. Month of maximum a) PE to EKE conversion b)  $\text{EKE}_{\leq 60\text{km}}$  and c)  $\text{EKE}_{60-300\text{km}}$ . Temporal lag, in months, between d) peak  $\text{EKE}_{\leq 60\text{km}}$  and peak PE to EKE conversion rate, and e)  $\text{EKE}_{\leq 60\text{km}}$  and  $\text{EKE}_{60-300\text{km}}$ . Green regions are those omitted from the lag calculation, including where the total seasonal range in EKE at  $< 300$  km scales is less than 20% of the annual mean EKE. White and light orange regions in (d) identify where the conversion from PE to EKE occurs at the same time or just prior to the peak in EKE at small scales. These regions correspond to the orange regions in (e) where the peak in EKE at large scales follows the peak in EKE at small scales by 1 to 4 months.



## b. Seasonal Variations of Available Potential Energy and Conversion to Kinetic Energy

The seasonal cycle in the PE to EKE conversion rate is independently estimated from observations to aid interpretation of EKE seasonality and scale-dependence. Temporally, this conversion rate exhibits a distinct peak during specific winter months, often aligning with  $EKE_{\leq 60km}$  (Fig. 5). Both the mean and seasonal amplitude of this estimated rate are elevated in subtropical western boundary current regions, the subpolar North Atlantic, and the Southern Ocean (Fig. 7), with the seasonal amplitude often larger than the annual mean. The PE to EKE conversion rate is a proxy for EKE generation at submesoscales. We argue that some of this submesoscale energy likely moves upscale, and thus that understanding seasonal modulations in the PE to EKE conversion rate are important in understanding and modeling mesoscale motions.

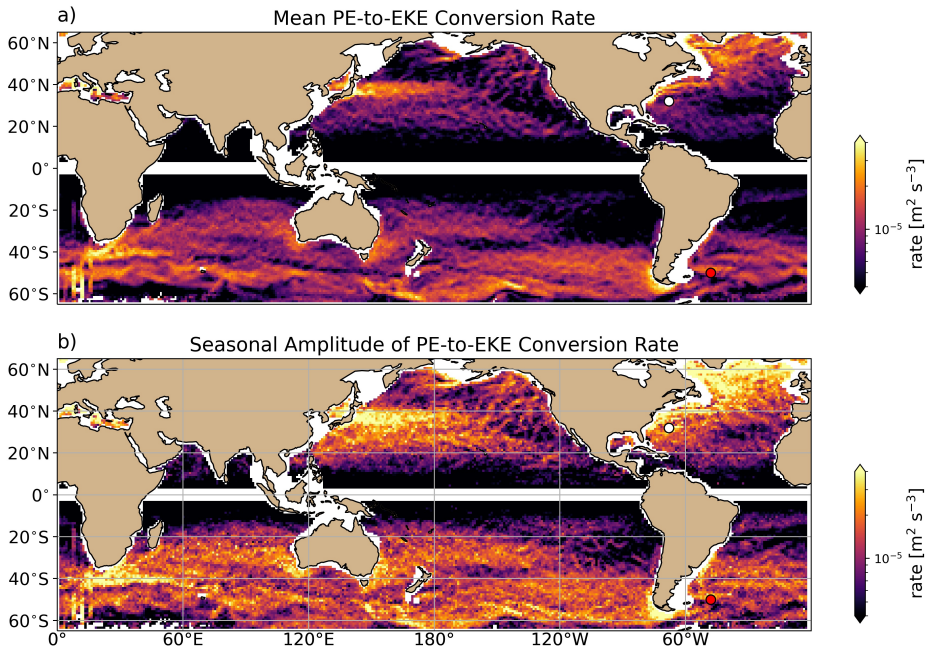


FIG. 7. a) Mean PE to EKE conversion rate. b) Seasonal amplitude (maximum - minimum) of the PE to EKE conversion rate.

To relate the seasonality of the PE to EKE conversion rate to that of small and larger-scale EKE, we first consider the seven locations highlighted in Figure 5. The PE to EKE conversion rate is elevated

380 in specific winter months, but remains non-zero throughout the year. This pattern is interpreted  
381 as an increased pool of available potential energy susceptible to baroclinic instability, which, as  
382 implied by Fox-Kemper et al. (2008), occurs principally at scales smaller than the deformation  
383 radius. At many locations, this expectation is corroborated by the fact that the conversion rate  
384 reaches its elevated wintertime level in the months preceding or at the same time as the peak EKE  
385 at scales less than 60 km. At sites where the PE to EKE conversion rate peaks before EKE at  
386 any scale, the subsequent progression in EKE across increasing scales follows (Fig. 5e,f,g,h). At  
387 sites where this does not occur, the seasonal cycles in mixed layer PE and EKE may be related via  
388 different dynamics such as a forward cascade of KE.

389 In general, if mixed layer instability generates small-scale EKE as quantified by Eq. 16 (Fig. 7),  
390 we would expect geographic overlap between regions with seasonality in PE to EKE conversion  
391 and EKE at small scales. If this EKE then moves to larger scales via the inverse cascade, we would  
392 expect geographic overlap among regions with seasonality in PE to EKE conversion, seasonality in  
393 EKE at small scales, *and* seasonally-lagged EKE at large scales. We first investigate the geographic  
394 overlap between where the seasonal amplitude of the conversion rate is greater than its annual mean  
395 (Fig. 7) and where the seasonal amplitude in EKE at 60 - 140 km scales, expressed as a fraction of  
396 total KE, is greater than its annual mean (Fig. 8a,b). These independently estimated quantities are  
397 both elevated throughout the mid-latitude gyres (Fig. 8b). Regions where this overlap occurs are  
398 interpreted as experiencing both a strong seasonal cycle in PE to EKE conversion and in resolved  
399 EKE at scales closest to those energized via the conversion of PE to KE. Within regions of this  
400 overlap, nearly 50% of EKE lag estimates (Fig. 8c) are between one and four months while  
401 outside of these regions, this percentage drops to less than 20%. We next compare regions where  
402 the seasonal amplitude of the PE to EKE conversion rate exceeds its annual mean and where we  
403 observe a positive lag of 1 to 4 months lag between peak  $EKE_{\leq 60km}$  and peak  $EKE_{60-300km}$  (Fig.  
404 8c,d). Again the mid-latitude gyres stand out as regions of overlap (Fig. 8d). The alignment of  
405 these overlap regions (Figure 8b,d) suggests a correspondence between the seasonal cycle in EKE  
406 across mesoscales and the presumed source of this energy: potential energy stored in the upper  
407 ocean. While we are unable to resolve EKE at and below deformation radius scales, spatial patterns  
408 in the lag between month of peak PE to EKE conversion and month of peak  $EKE_{\leq 60km}$  align with  
409 regions where we also observe a 1 to 4 month lag between  $EKE_{\leq 60km}$  and  $EKE_{60-300km}$ .



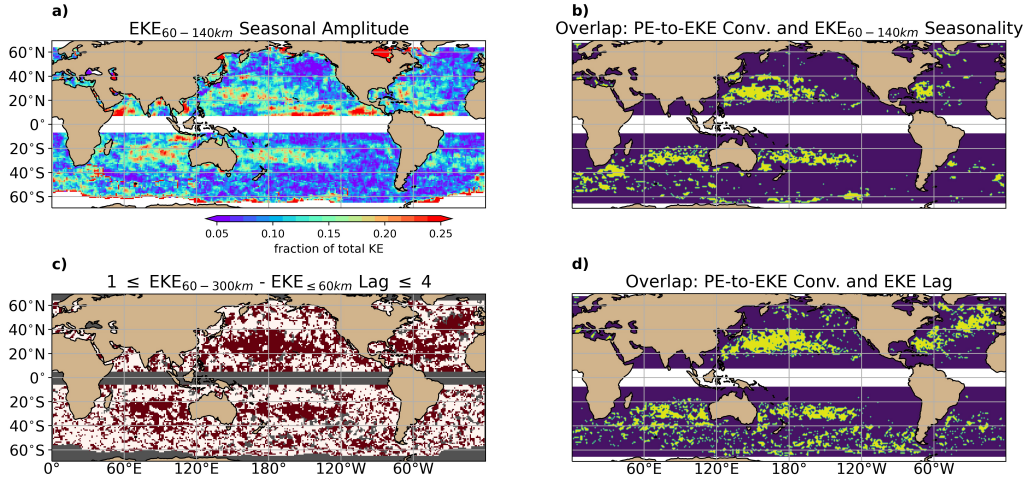


FIG. 8. a) Seasonal amplitude of the fraction of kinetic energy within the 60 - 140 km wavelength band. b) Regions (yellow) where the seasonal amplitudes in the PE to EKE conversion rate and fraction of EKE<sub>60-140km</sub> exceed their annual mean values. c) Regions (red) where the lag between peak EKE<sub>≤60km</sub> and EKE<sub>60-300km</sub> is greater than or equal to 1 month and less than or equal to 4 months. d) Regions (yellow) where the seasonal amplitude in the PE to EKE conversion rate exceeds the annual mean and EKE lags fall between 1 and 4 months.

## 5. Discussion

### a. Interpretation as an inverse cascade

We interpret these results as indirect observation of the inverse cascade through two pieces of evidence. The first is a 1 to 4 month lag between the seasonal peak of EKE<sub>≤60km</sub> and EKE<sub>60-300km</sub>. The second is that seasonality in an independent estimate of PE to EKE conversion peaks at the same time as small-scale EKE, and is elevated in regions where EKE lags are positive. Overall, observed PE to EKE<sub>≤60km</sub> lags of 0-2 months and EKE<sub>≤60km</sub> to EKE<sub>60-300km</sub> lags of 1-4 months occur in overlapping regions (Fig. 6d,e). In these regions, we identify a progression in the month of peak PE to EKE conversion, EKE<sub>≤60km</sub>, EKE<sub>≤140km</sub>, and finally EKE<sub>≤300km</sub>. These features are consistent with high-resolution modeling studies which explicitly diagnose seasonality in the strength of the inverse cascade (Qiu et al. 2014; Sasaki et al. 2014; Uchida et al. 2017).

426 It is presumed that seasonal mixed layer PE, deriving from wintertime mixed layer deepening  
 427 and elevated horizontal buoyancy gradients, is a source of EKE predominantly at scales smaller  
 428 than those resolved by along-track altimeter observations. Where an inverse cascade is local and  
 429 moves this energy to larger scales, we expect geographic alignment in the PE to EKE conversion  
 430 rate and small-scale EKE resolved here. This expectation is tested by considering the intersection  
 431 of regions where the seasonal cycle in the rate of PE to EKE conversion is large and where  
 432 significant seasonality in EKE at 60-140 km scales is observed (Fig. 8b). The resulting overlap  
 433 suggests a dynamical correspondence between these independent observations linking the reservoir  
 434 of available potential energy in the upper ocean, strong seasonality in small-scale EKE, and a  
 435 progression in the month of peak EKE first at small and then large scales. These observations  
 436 reveal an energy cycle that can be sequentially interpreted as: a wintertime increase in PE to EKE  
 437 conversion, driven by deeper wintertime mixed layers susceptible to baroclinic instability in the  
 438 presence of stronger lateral buoyancy gradients, followed by elevated eddy activity at scales less  
 439 than or equal to the first baroclinic deformation radius (Smith 2007), and finally an inverse cascade  
 440 of KE up to altimeter-resolved scales evidenced by a lag in the month of peak  $EKE_{\leq 60km}$  preceding  
 441 that of  $EKE_{60-300km}$ .

442 Geographic patterns in PE to EKE conversion specifically align with regions where a majority  
 443 of springtime restratification is generated via the lateral slumping of horizontal density gradients  
 444 (Johnson et al. 2016). In their analysis, Johnson et al. (2016) discuss the contribution to this  
 445 conversion of horizontal density gradients to vertical density gradients by mixed layer eddies  
 446 (Figure 4 of Johnson et al. (2016)). The formation of these eddies, representing the conversion of  
 447 PE to EKE, in regions where we observe a 0-2 month lag between peak PE to EKE conversion and  
 448  $EKE_{\leq 60km}$  (Fig. 6d) lends support to our interpretation that the smallest scale EKE observed by  
 449 the altimeter reflects energy derived from mixed layer baroclinic instability. The relatively short  
 450 lag suggests this energy moves upscale at the  $\sim 1$ -month time scale. This result is consistent with  
 451 Uchida et al. (2017), who calculated a 40 - 50 day eddy turnover time scale for regions with elevated  
 452 eddy activity. In these same regions we observe a lag of 1 to 4 months between peak EKE at  $\leq$   
 453 60 km scales and between 60 - 300 km scales. Interpreted together, these regions identify where  
 454 geostrophic turbulence drives an inverse cascade from submeso- through mesoscales. Note that  
 455 these regions are a conservative estimate of where the inverse cascade occurs. It may additionally

456 be present in other locations with decreased seasonality or at a faster pace such that no perceptible  
457 time lag is identified from monthly observations.

458 Several studies have documented a link between mixed layer instability and mesoscale eddy ki-  
459 netic energy. Using a high resolution realistic numerical simulation of the North Pacific, Sasaki et al.  
460 (2014) consider additional sources, including Charney-like and Phillips-like instability processes,  
461 and conclude that seasonally-varying mixed layer instability is a dominant source of mesoscale  
462 EKE. Both high resolution simulations (Mensa et al. 2013), and observations in the North Atlantic  
463 (Callies et al. 2015), have shown a correspondence between mixed layer depth and submesoscale  
464 EKE. This correspondence aligns with the temporal patterns of mixed layer PE and small-scale  
465 EKE shown here.

466 Other sources of mesoscale KE are considered unlikely to cause the pattern of lag shown here.  
467 Investigating the temporal offset between seasonal cycles of EKE and its presumed energy source  
468 mechanism, baroclinic instability, Zhai et al. (2008) rule out seasonal variations in Ekman pumping  
469 as a driver of EKE seasonality. Their results can be reinterpreted by acknowledging that their  
470 observed summertime peak in EKE is defined relative to a temporal mean. This likely corresponds  
471 to peak EKE at large scales while small-scale EKE, contributing less to total KE, peaks earlier in  
472 the year and closer to their observed time of peak eddy growth rate. Other sources of mesoscale  
473 KE that may be seasonally varying, like large-scale wind forcing or baroclinic instability at scales  
474 greater than the deformation radius, are considered unlikely to cause the pattern of lag shown here.  
475 Wind forcing and its seasonal variability largely occur at basin scales and although surface ocean  
476 temperature fronts can alter the wind field at mesoscales, these feedbacks don't appear to have  
477 widespread seasonal scale-dependence (Risien and D.B 2008; Serazin et al. 2018).

478 In high resolution simulations south of the Kuroshio, Sasaki et al. (2014) and Qiu et al. (2014)  
479 consider mesoscale KE and the influence of interior baroclinic instability. Authors conclude that  
480 contributions to larger scale KE include a seasonally dependent upscale cascade as well as a  
481 persistent source of EKE associated with vertically sheared mean flows. However, the seasonal  
482 amplitude of KE at these larger scales associated with interior instability is weaker than that at  
483 smaller scales. Sasaki et al. (2014) conclude from this that most of the KE in the mesoscale band  
484 is affected by seasonality generated in wintertime at submesoscales.

485 Implicit in these arguments is the assumption that SSH anomalies used in estimating KE reflect  
486 predominantly balanced motions. Qiu et al. (2014) identify spatial variability in the transition scale  
487 between balanced and unbalanced motions, revealing much of the EKE at mid-latitudes, especially  
488 within the western halves of ocean basins, to reflect balanced motions. These regions again align  
489 with those here associated with a lag in the peak month of EKE, suggesting that the progression in  
490 EKE is not the result of seasonally varying unbalanced motions. The correspondence of locations  
491 of lag in EKE from smaller to larger scales and locations of both increased wintertime mixed layer  
492 PE conversion and small-scale EKE provide additional support to the argument that these lags  
493 identify regions where geostrophic turbulence moves energy from smaller to larger scales.

#### 494 *b. Implications and practical applications*

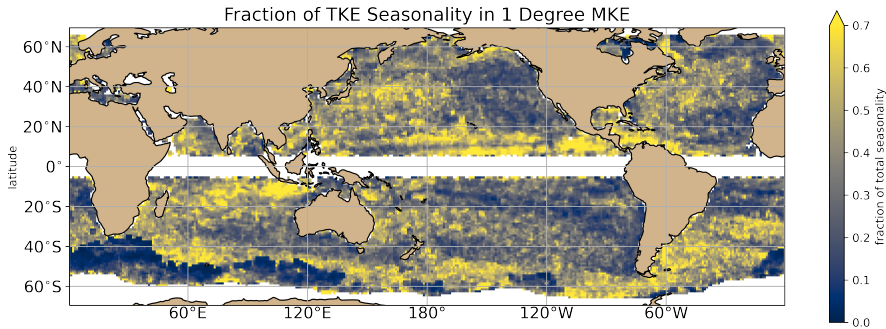
495 The generalized spatial filtering framework applied here is applicable to any along-track observa-  
496 tion. Satellite, time window, filter length scale including degree or kilometer options, filter kernel,  
497 and gridding scheme parameters can be varied in this scale-aware framework to explore specific  
498 questions or compare to model output. A resulting dataset and example code have been made  
499 publicly available, and we encourage its use. As a contribution to the current Ocean Transport  
500 and Eddy Energy Climate Process Team (Zanna 2019; Cole et al. 2020), this analysis framework  
501 is intended to aid in efforts to partition energy across reservoirs and regulate cross-scale transfers  
502 using parameterizations.

503 Comparison of boxcar, Gaussian, and taper filters reveals the taper filter as the sharpest in spectral  
504 space. As a low-pass filter with a cutoff wavelength of  $L_f$ , this kernel most closely approximates a  
505 step-function in wavenumber space (Fig. 1c). Use of this filter thus produces a field with the least  
506 smearing of wavelengths across scales. The effect of this design and result of its implementation,  
507 as compared to equivalent analysis using a Gaussian filter kernel, reveal a more distinct signal of  
508 seasonality in EKE at different scales. In particular, the month of peak EKE at any given scale is  
509 more pronounced and sometimes different for the taper filter than the Gaussian filter (Fig. 1d).

510 This framework and data processing can be applied to filtered sea level anomaly, cross-track  
511 geostrophic velocity, or an arbitrary 1-D scalar field across multiple scales using a desired filter  
512 kernel. If afforded by horizontal resolution, the filter scale can be selected to spatially vary with  
513 the local first baroclinic radius of deformation (Chelton et al. 1998). Applying this variable filter

514 to geostrophic velocity results in estimates of EKE at scales less than those at which mesoscale  
515 eddies are expected to equilibrate, and also quantifies energy at scales greater than the deformation  
516 radius and within the realm of geostrophic turbulence. Selection of a filter scale tied to a model  
517 grid scale, however, allows for direct comparisons between observations and models that have  
518 geographically-varying grid scales. This may be particularly relevant for models that may only  
519 resolve eddies regionally, depending on their effective resolution relative to the local scale at which  
520 eddies equilibrate (Hallberg 2013).

521 As an example of how this filtering framework can be used to gauge resolved seasonality in  
522 a global climate model with relatively coarse resolution, we filter along-track velocities using a  
523 spatial filter kernel of width equal locally to 1 degree of longitude. Comparison of seasonality  
524 in the resulting MKE estimate to that of the unfiltered KE (Fig. 9) shows that while nearly ~  
525 60% of the seasonal change in total KE is resolved in western boundary current regions, this is  
526 reduced to less than a third in the eastern half of the main ocean basins. Together with the observed  
527 seasonality in PE to EKE conversion that is greater than the annual mean, these results stress the  
528 need to implement time-varying parameterizations for energy conversion (such as Eq. 16), as well  
529 as those for sub-grid scale EKE.



530 FIG. 9. Fraction of total kinetic energy seasonality resolved in 1 degree MKE estimate. This quantity is the  
531 ratio (filtered/total) of maximum - minimum kinetic energy across a seasonal cycle.

## 6. Conclusions

We identify stastically significant geographic and seasonal variations in eddy kinetic energy using a spatial filtering framework applied to along-track satellite altimeter derived estimates of geostrophic velocity. The partitioning of kinetic energy across spatial scales into mean and eddy components reveals a large fraction of total energy falls within the mesoscale band (60 - 300 km), varying with latitude and increasing with proximity to western boundary currents. This analysis also reveals that most regions of the ocean exhibit a winter-to-summer change in KE of  $\sim 20\%$  for scales of 60-140 km (Fig. 4), while seasonal peaks at 140-300 km scales occur over a range of months and depend on the local energy transfer pathways. These results highlight a scale-dependent seasonal cycle in eddy kinetic energy observed primarily at mid-latitudes where large scales attain a seasonal maximum in the months following small scales, consistent with an inverse energy cascade.

The presence and seasonality of an inverse energy cascade is confirmed from concurrent estimates of seasonality in the conversion of potential energy to kinetic energy via mixed layer instability. The mean PE to EKE conversion rate, estimated via a parameterization (Fox-Kemper et al. 2008), is elevated at mid-latitudes, with the peak conversion rate occurring typically in mid-winter (Fig. 5). At most locations the seasonal amplitude in this conversion rate is larger than its annual average.

Taken together, the temporal and geographic patterns of the PE to EKE conversion rate and EKE across spatial scales reveal a seasonally varying inverse cascade throughout the subtropical gyres. The geographic co-location of seasonality in each of these components of the energy cascade (conversion rate, small-scale, and large-scale EKE) as well as seasonal timing consistent with an energy cascade supports this conclusion. The timing in particular of PE to EKE conversion and maximum EKE at 60-140 km scales suggests kinetic energy released via mixed layer instability is a source of mesoscale kinetic energy moving upscale throughout late winter months. We have conservatively estimated the regions in which an inverse cascade occurs, and it is possible that some of the regions where a lag of zero months is observed also contain an energy cascade that occurs more rapidly than the regions identified here. We are able to identify regions where the total time lag between PE to EKE conversion and large-scale EKE is 1-6 months (0-2 month lag to small-scale EKE followed by a 1-4 month lag to large-scale EKE). While we are limited by the  $\sim 50$  km resolution of along-track satellite observations, it may be possible that an inverse

562 cascade exists at smaller spatial scales in some locations, particularly higher latitudes where the  
563 deformation radius is smaller. These results, specifically a scale dependent seasonal cycle in EKE  
564 linked to seasonality in the conversion of PE to EKE, confirm similar seasonal energy cycles seen  
565 in high resolution models (Uchida et al. 2017).

566 A widespread inverse cascade has implications spanning the water column. If some portion of  
567 wintertime submesoscale kinetic energy in the mixed layer energizes the mesoscale, then restrat-  
568 ification of the mixed layer and related biological processes, like the springtime phytoplankton  
569 bloom, could depend on this inverse cascade and its timescale (Mahadevan et al. 2012). Where  
570 energy moves from smaller to larger horizontal scales, a similar cascade is also expected in the  
571 vertical, resulting in the barotropization, or transfer of energy to greater depths, of eddy vertical  
572 structures (Smith and Vallis 2001). Where barotropization is enhanced, so too may be bottom  
573 velocities that drive dissipation at the sea floor. In general, an improved understanding of pro-  
574 cesses controlling mesoscale energy levels, as well as cascade rates across space and time scales,  
575 is needed to predict and model ocean energetics. These questions, along with investigations of the  
576 steady-state component of the inverse cascade, are left for future studies.

577 In addition to these results, the importance of a scale-aware view of the ocean's kinetic energy  
578 resides in its use as a validation metric for numerical models that resolve, partially resolve, or  
579 parameterize kinetic energy sources and sinks. The scale-aware and customizable nature of the  
580 one-dimensional analysis tool developed here provides the flexibility needed for a comprehensive  
581 evaluation of mesoscale processes in a range of numerical models. Using this tool to explore  
582 seasonality reveals the prevalence of an inverse cascade and stresses the importance of adequately  
583 resolving or parameterizing mesoscale eddy activity in global climate models. It is critical that  
584 energy in these models is properly partitioned across scales, locations, and seasons, as mesoscale  
585 turbulence redistributes heat and nutrients under the influence of changing large-scale circulation  
586 patterns.

587 *Acknowledgments.* This work was generously funded by NSF grants OCE-1912302, OCE-  
588 1912125 (Drushka), and OCE-1912325 (Abernathey) as part of the Ocean Energy and Eddy  
589 Transport Climate Process Team. We would like to thank Laure Zanna and the rest of the team for  
590 their feedback, guidance, and support.

591 *Data availability statement.* All altimeter measurements employed in this analysis can be obtained  
592 on Pangeo Abernathey et al. (2021) [[https://catalog.pangeo.io/browse/master/ocean/  
593 altimetry/](https://catalog.pangeo.io/browse/master/ocean/altimetry/)] and are pre-processed for easy access. As presented here, filtering can be applied and  
594 scale-aware MKE and EKE estimated from Jason-2, SARAL-AltiKa, and Sentinel-3A along-track  
595 measurements using examples provided on github [[https://github.com/ocean-eddy-cpt/  
596 WP1T2-2D-EKE-Analysis/along\\_track\\_filtering.ipynb](https://github.com/ocean-eddy-cpt/WP1T2-2D-EKE-Analysis/along_track_filtering.ipynb)]. This repository also contains  
597 ready-made maps of EKE defined for various filter scales and types. Data files corresponding  
598 to filtering with Gaussian and taper filters in kilometers have been made available in NetCDF  
599 format (DOI data citation to be added prior to final acceptance). Gridded climatology of upper  
600 ocean density and mixed layer depth is generated from databases of Argo derived temperature and  
601 salinity profiles (Roemmich and Gilson 2009) [[http://sio-argo.ucsd.edu/RG\\_Climatology.html](http://sio-argo.ucsd.edu/RG_Climatology.html)],  
602 as well as mixed layer depths (Holte et al. 2017). These data were collected and made freely  
603 available by the International Argo Program and the national programs that contribute to it  
604 [<http://www.argo.ucsd.edu>]. The Argo Program is part of the Global Ocean Observing System.

## 605 **References**

- 606 Abernathey, R., and Coauthors, 2021: Cloud-native repositories for big scientific data. *Computing  
607 in Science & Engineering*, **23**, 26–35, <https://doi.org/10.1109/MCSE.2021.3059437>.
- 608 Aluie, H., M. Hecht, and G. Vallis, 2018: Mapping the energy cascade in the north atlantic ocean:  
609 The coarse-graining approach. *Journal of Physical Oceanography*, **48**, 225–244, [https://doi.org/  
610 https://doi.org/10.1175/JPO-D-17-0100.1](https://doi.org/https://doi.org/10.1175/JPO-D-17-0100.1).
- 611 Arbic, B., M. Muller, J. Richman, J. Shriver, A. Morten, R. Scott, G. Serazin, and T. Pen-  
612 duff, 2014: Geostrophic turbulence in the wavenumber-frequency domain: Eddy-driven low-  
613 frequency variability. *Journal of Physical Oceanography*, **44**, 2050–2069, [https://doi.org/  
614 https://doi.org/10.1175/JPO-D-13-054.1](https://doi.org/https://doi.org/10.1175/JPO-D-13-054.1).



Arbic, B., K. Polzin, R. Scott, J. Richman, and J. Shriver, 2013: On eddy viscosity, energy cascades, and the horizontal resolution of gridded satellite altimeter products. *Journal of Physical Oceanography*, **43**, 283–300, [https://doi.org/https://doi.org/10.1175/JPO-D-11-0240.1](https://doi.org/10.1175/JPO-D-11-0240.1).

Arbic, B., R. Scott, D. Chelton, J. Richman, and J. Shriver, 2012: Effects of stencil width on surface ocean geostrophic velocity and vorticity estimation from gridded satellite altimeter data. *Journal of Geophysical Research*, **117**, [https://doi.org/https://doi.org/10.1029/2011JC007367](https://doi.org/10.1029/2011JC007367).

Callies, J., and R. Ferrari, 2013: Interpreting energy and tracer spectra of upper-ocean turbulence in the submesoscale range (1–200 km). *Journal of Physical Oceanography*, **43**, 2456–2474, [https://doi.org/https://doi.org/10.1175/JPO-D-13-063.1](https://doi.org/10.1175/JPO-D-13-063.1).

Callies, J., R. Ferrari, J. Klymak, and J. Gula, 2015: Seasonality in submesoscale turbulence. *Nature Communications*, **6**, [https://doi.org/https://doi.org/10.1038/ncomms7862](https://doi.org/10.1038/ncomms7862).

Callies, J., G. Flierl, R. Ferrari, and B. Fox-Kemper, 2016: The role of mixed-layer instabilities in submesoscale turbulence. *Journal of Fluid Mechanics*, **788**, 5–41, <https://doi.org/10.1017/jfm.2015.700>.

Charney, J., 1971: Geostrophic turbulence. *Journal of the Atmospheric Sciences*, **28**, 1087–1095.

Chelton, D., R. deSzoek, M. Schlax, K. El Naggar, and N. Siwertz, 1998: Geographical variability of the first-baroclinic Rossby radius of deformation. *Journal of Physical Oceanography*, **28**, 433–460, [https://doi.org/https://doi.org/10.1175/1520-0485\(1998\)028<0433:GVOTFB>2.0.CO;2](https://doi.org/10.1175/1520-0485(1998)028<0433:GVOTFB>2.0.CO;2).

Chelton, D., M. Schlax, R. Samelson, and R. de Szoek, 2007: Global observations of large oceanic eddies. *Geophysical Research Letters*, **34**, [https://doi.org/https://doi.org/10.1029/2007GL030812](https://doi.org/10.1029/2007GL030812).

Chelton, D., M. Schlax, R. Samelson, and R. de Szoek, 2011: Global observations of nonlinear mesoscale eddies. *Progress in Oceanography*, **91**, 167–216, [https://doi.org/https://doi.org/10.1016/j.pocean.2011.01.002](https://doi.org/10.1016/j.pocean.2011.01.002).

Chen, S., and B. Qiu, 2021: Sea surface height variability in the 30–120 km wavelength band from altimetry along-track observations. *Journal of Geophysical Research: Oceans*, [https://doi.org/https://doi.org/10.1029/2021JC017284](https://doi.org/10.1029/2021JC017284).

642 Cole, S., K. Drushka, and R. Abernathey, 2020: Toward an observational synthesis of eddy energy  
 643 in the global ocean. *CLIVAR Exchanges / US CLIVAR Variations*, **18**, 37–41, [https://doi.org/](https://doi.org/10.5065/g8w0-fy32)  
 644 10.5065/g8w0-fy32.

645 Dong, J., B. Fox-Kemper, H. Zhang, and C. Dong, 2020a: The scale of submesoscale baroclinic  
 646 instability globally. *Journal of Physical Oceanography*, **50**, 2649–2667, [https://doi.org/10.1175/](https://doi.org/10.1175/JPO-D-20-0043.1)  
 647 JPO-D-20-0043.1.

648 Dong, J., B. Fox-Kemper, H. Zhang, and C. Dong, 2020b: The seasonality of submesoscale  
 649 energy production, content, and cascade. *Geophysical Research Letters*, <https://doi.org/https://doi.org/10.1029/2020GL087388>.

651 Dufau, C., M. Orszynowicz, G. Dibarboue, R. Morrow, and P. Le Traon, 2016: Mesoscale  
 652 resolution capability of altimetry: Present and future. *Journal of Geophysical Research: Oceans*,  
 653 **121**, 4910–4927, <https://doi.org/https://doi.org/10.1002/2015JC010904>.

654 Ferrari, R., and C. Wunsch, 2009: Ocean circulation kinetic energy: Reservoirs, sources,  
 655 sinks. *Annual Review of Fluid Mechanics*, [https://doi.org/https://doi.org/10.1146/annurev.fluid.](https://doi.org/https://doi.org/10.1146/annurev.fluid.40.111406.102139)  
 656 40.111406.102139.

657 Fox-Kemper, B., R. Ferrari, and R. Hallberg, 2008: Parameterization of mixed layer eddies. part  
 658 i: Theory and diagnosis. *Journal of Physical Oceanography*, **38**, 1145–1165, [https://doi.org/](https://doi.org/10.1175/2007JPO3792.1)  
 659 10.1175/2007JPO3792.1.

660 Fox-Kemper, B., and Coauthors, 2011: Parameterization of mixed layer eddies. iii: Implementation  
 661 and impact in global ocean climate simulations. *Ocean Modelling*, **39**, 61–78, [https://doi.org/](https://doi.org/10.1016/j.ocemod.2010.09.002)  
 662 10.1016/j.ocemod.2010.09.002.

663 Germano, M., 1992: Turbulence: The filtering approach. *Journal of Fluid Mechanics*, **238**, 325–  
 664 336.

665 Grooms, I., N. Loose, R. Abernathey, J. Steinberg, S. Bachman, G. Marques, A. Guillaumin,  
 666 and E. Yankovsky, 2021: Diffusion-based smoothers for spatial filtering of gridded geophysical  
 667 data. *Journal of Advances in Modeling Earth Systems*, [https://doi.org/https://doi.org/10.1029/](https://doi.org/https://doi.org/10.1029/2021MS002552)  
 668 2021MS002552.

669 Hallberg, R., 2013: Using a resolution function to regulate parameterizations of oceanic mesoscale  
670 eddy effects. *Ocean Modelling*, **72**, 92–103, [https://doi.org/https://doi.org/10.1016/j.ocemod.](https://doi.org/https://doi.org/10.1016/j.ocemod.2013.08.007)  
671 2013.08.007.

672 Holte, J., L. Talley, J. Gilson, and D. Roemmich, 2017: An argo mixed layer climatol-  
673 ogy and database. *Geophysical Research Letters*, **44**, 5618–5626, [https://doi.org/10.1002/](https://doi.org/10.1002/2017GL073426)  
674 2017GL073426.

675 Johnson, L., C. Lee, and E. D’Asaro, 2016: Global estimates of lateral springtime restratification.  
676 *Journal of Physical Oceanography*, **46**, 1555–1573, <https://doi.org/10.1175/JPO-D-15-0163.1>.

677 Kraichnan, R., 1967: Inertial ranges in two-dimensional turbulence. *The Physics of Fluids*, **10**,  
678 1417–1423, <https://doi.org/https://doi.org/10.1063/1.1762301>.

679 Mahadevan, A., E. D’Asaro, C. Lee, and M. Perry, 2012: Eddy-driven stratification initiates north  
680 atlantic spring phytoplankton blooms. *Science*, **337**, 54–58, [https://doi.org/10.1126/science.](https://doi.org/10.1126/science.1218740)  
681 1218740.

682 Matano, R., C. Simionato, W. de Ruijter, P. Van Leeuwan, P. Strub, D. Chelton, and M. Schlax,  
683 1998: Seasonal variability in the agulhas retroflexion region. *Geophysical Research Letters*, **25**,  
684 4361–4364, <https://doi.org/https://doi.org/10.1029/1998GL900163>.

685 McWilliams, J., 1989: Statistical properties of decaying geostrophic turbulence. *Journal of Fluid*  
686 *Mechanics*, **198**, 199–230, <https://doi.org/10.1017/S0022112089000108>.

687 Mensa, J., Z. Garraffo, A. Griffa, T. Ozgokmen, A. Haza, and M. Veneziani, 2013: Seasonality  
688 of the submesoscale dynamics in the gulf stream region. *Ocean Dynamics*, [https://doi.org/](https://doi.org/https://doi.org/10.1007/s10236-013-0633-1)  
689 <https://doi.org/10.1007/s10236-013-0633-1>.

690 Pujol, M., and F. Mertz, 2020: Product user manual for sea level sla products (cmems-sl-pum-009-  
691 032-062). *Copernicus Marine Environment Monitoring System*.

692 Qiu, B., S. Chen, P. Klein, H. Sasaki, and S. Y., 2014: Seasonal mesoscale and submesoscale eddy  
693 variability along the north pacific subtropical countercurrent. *Journal of Physical Oceanography*,  
694 **44**, 3079–3098, <https://doi.org/https://doi.org/10.1175/JPO-D-14-0071.1>.

- 695 Risien, C., and C. D.B, 2008: A global climatology of surface winds and surface wind stress  
696 fields from eight years of quikscat scatterometer data. *Journal of Physical Oceanography*,  
697 <https://doi.org/https://doi.org/10.1175/2008JPO3881.1>.
- 698 Rocha, C., T. Chereskin, S. Gille, and D. Menemenlis, 2016: Mesoscale to submesoscale wavenum-  
699 ber spectra in drake passage. *Journal of Physical Oceanography*, **46**, 601–620, [https://doi.org/](https://doi.org/https://doi.org/10.1175/JPO-D-15-0087.1)  
700 <https://doi.org/10.1175/JPO-D-15-0087.1>.
- 701 Roemmich, D., and J. Gilson, 2009: The 2004–2008 mean and annual cycle of temperature, salinity,  
702 and steric height in the global ocean from the argo platform. *Progress in Oceanography*, **82**,  
703 81–100.
- 704 Roulet, G., J. McWilliams, X. Capet, and M. Molemaker, 2012: Properties of steady  
705 geostrophic turbulence with isopycnal outcropping. *Journal of Physical Oceanography*, **42**,  
706 18–38, <https://doi.org/https://doi.org/10.1175/JPO-D-11-09.1>.
- 707 Sadek, M., and H. Aluie, 2018: Extracting the spectrum by spatial filtering. *Physical Review*  
708 *Fluids*, **3**, <https://doi.org/https://doi.org/10.1103/PhysRevFluids.3.124610>.
- 709 Sasaki, H., P. Klein, B. Qiu, and Y. Sasai, 2014: Impact of oceanic-scale interactions on the seasonal  
710 modulation of ocean dynamics by the atmosphere. *Nature Communications*, [https://doi.org/](https://doi.org/https://doi.org/10.1038/ncomms6636)  
711 <https://doi.org/10.1038/ncomms6636>.
- 712 Scharffenberg, M., and D. Stammer, 2010: Seasonal variations of the large-scale geostrophic flow  
713 field and eddy kinetic energy inferred from the topex/poseidon and jason-1 tandem mission data.  
714 *Journal of Geophysical Research*, **115**, 3523–3537, <https://doi.org/10.1029/2008JC005242>.
- 715 Scott, R., and B. Arbic, 2007: Spectral energy fluxes in geostrophic turbulence: Implications  
716 for ocean energetics. *Journal of Physical Oceanography*, **37**, 673–688, <https://doi.org/https://doi.org/10.1175/JPO3027.1>.
- 717  
718 Scott, R., and F. Wang, 2005: Direct evidence of an oceanic inverse kinetic energy cascade  
719 from satellite altimetry. *Journal of Physical Oceanography*, **35**, 1650–1666, [https://doi.org/](https://doi.org/https://doi.org/10.1175/JPO2771.1)  
720 <https://doi.org/10.1175/JPO2771.1>.
- 721 Serazin, G., T. Penduff, B. Barnier, J. Molines, B. Arbic, M. Muller, and L. Terray, 2018: In-  
722 verse cascades of kinetic energy as a source of intrinsic variability: A global ogcm study.

*Journal of Physical Oceanography*, **48**, 1385–1408, <https://doi.org/https://doi.org/10.1175/JPO-D-17-0136.1>.

Smith, K., 2007: The geography of linear baroclinic instability on earth's oceans. *Journal of Marine Research*, **65**, 655–683, <https://doi.org/10.1357/002224007783649484>.

Smith, K., and G. Vallis, 2001: The scales and equilibrium of midocean eddies: Freely evolving flow. *Journal of Physical Oceanography*, **31**, 554–571, [https://doi.org/https://doi.org/10.1175/1520-0485\(2001\)031<0554:TSAEOM>2.0.CO;2](https://doi.org/https://doi.org/10.1175/1520-0485(2001)031<0554:TSAEOM>2.0.CO;2).

Stammer, D., and C. Dieterich, 1999: Space-borne measurements of the time-dependent geostrophic ocean flow field. *Journal of Atmospheric and Oceanic Technology*, **16**, 1198–1207, [https://doi.org/https://doi.org/10.1175/1520-0426\(1999\)016<1198:SBMOTT>2.0.CO;2](https://doi.org/https://doi.org/10.1175/1520-0426(1999)016<1198:SBMOTT>2.0.CO;2).

Taburet, G., M. Pujol, and S.-T. team, 2020: Quality information document: Sea level tac - duacs products (cmems-sl-quid-008-032-062). *Copernicus Marine Environment Monitoring System*.

Uchida, T., R. Abernathey, and S. Smith, 2017: Seasonality of eddy kinetic energy in an eddy permitting global climate model. *Ocean Modelling*, **118**, 41–58, <https://doi.org/https://doi.org/10.1016/j.ocemod.2017.08.006>.

Xu, Y., and L. Fu, 2012: The effects of altimeter instrument noise on the estimation of the wavenumber spectrum of sea surface height. *Journal of Physical Oceanography*, **42**, 2229–2233, <https://doi.org/https://doi.org/10.1175/JPO-D-12-0106.1>.

Zanna, L., 2019: Proposal to cyp climate processs teams on “ocean transport and eddy energy”. *figshare*, <https://doi.org/https://doi.org/10.6084/m9.figshare.10105922.v1>.

Zhai, X., R. Greatbatch, and J. Kohlmann, 2008: On the seasonal variability of eddy kinetic energy in the gulf stream region. *Geophysical Research Letters*, <https://doi.org/https://doi.org/10.1029/2008GL036412>.